Granular Matter (2019) 21:101
https://doi.org/10.1007/s10035-019-0960-0

ORIGINAL PAPER

Pressure-dependent grain dissolution using discrete element simulations

Minsu Cha[1] · **J. Carlos Santamarina**[2]

Received: 30 December 2015

Abstract
Pressure solution-precipitation is a diagenetic process often involved in compaction, hardening, creep and healing. This study explores the evolution of pressure-dependent mineral dissolution using the discrete element method where grains are gradually contracted in proportion to the total normal force they carry. Under zero lateral strain and constant vertical stress boundary conditions, contact forces homogenize during the early stages of dissolution, there is a minor increase in coordination number and the global porosity decreases (even though there is no reprecipitation in these simulations). There is a transient drop in the lateral stress, shear bands start to emerge as the horizontal stress reaches a minimum value. The porosity is higher and the coordination number is lower within shear bands than in the surrounding soil wedges; furthermore, interparticle forces tend to homogenize within wedges, while marked force chains develop within shear bands. On the other hand, there is no shear localization during pressure solution simulations under isotropic stress boundary conditions. Regardless of the boundary conditions, the initially uniform grain size distribution evolves towards a unimodal distribution; improved particle grading facilitates the global reduction in porosity and the associated increase in coordination number. The emergence of shear discontinuities during pressure solution under zero lateral strains may explain the non-tectonic origin of polygonal fault systems observed in marine sediments and lacustrine deposits.

Keywords Grain dissolution · Pressure solution · Discrete element modeling · Shear localization · Polygonal faults

1 Introduction

Dissolution is a salient diagenetic process in sediments. Pressure solution involves the preferential dissolution of minerals at grain contacts followed by diffusive mass transfer to the surrounding pore space. Dissolved species either reprecipitate onto nearby stress-free surfaces [25, 48], or are advectively transported away through the porous network [23].

Pressure solution contributes to sediment compaction and porosity reduction [2, 13, 56]. It is an important mechanism in soil and rock creep [31, 36], and in ductile rock deformation in the upper crust [21, 22, 28, 34, 48]. Furthermore, pressure solution facilitates fault healing and strength recovery between seismic events [3, 40, 53, 62]. Stylolites are the most well-known feature of localized dissolution and volume reduction driven by pressure solution [5, 44, 58].

Pressure solution results from differences in the surface chemical potential between the mineral at contacts and the stress-free mineral [27, 34, 49]. Consequently, pressure solution responds to effective stress, either linearly [17, 29, 41, 45, 48], or as an exponential function of effective stress [20, 27].

Typically, pressure solution is favored at high temperatures [48] and fluid pressures [55], and in more reactive minerals (Note: carbonate solubility decreases with temperature). Small grain sizes of high specific surface increase the rate of pressure solution [16, 39, 45, 55].

Electronic supplementary material The online version of this article (https://doi.org/10.1007/s10035-019-0960-0) contains supplementary material, which is available to authorized users.

✉ Minsu Cha
mcha@tamu.edu

J. Carlos Santamarina
carlos.santamarina@kaust.edu.sa

[1] Zachry Department of Civil and Environmental Engineering, Texas A&M University, College Station, TX 77843, USA

[2] Earth Science and Engineering, King Abdullah University of Science and Technology (KAUST), Thuwal 23955-6900, Saudi Arabia

In this study, we explore pressure-dependent mineral dissolution at the scale of the granular skeleton. We use the discrete element method, DEM to investigate the underlying chemo-mechanical coupling and possible emergent phenomena. A description of the numerical approach follows.

2 Methodology

Discrete element simulations are conducted in 2D and 3D using PFC (ITASCA Consulting Group, Inc.—[14]. Table 1 describes the properties of the simulation environment for 2D and 3D cases, and the scope of the parametric study. While the 2D simulations facilitate the interpretation and visualization of results, all key observations extracted from this study apply to both 2D and 3D. Zero lateral strain boundaries are imposed to model the one-dimensional compaction of shallow uncemented sediments [57], and the upper boundary is either a constant stress or stress-free surface.

The 2D circular disks or 3D spheres are generated with an initial size equal to half their final size, and placed at random locations in a closed container. All grains then grow at the same rate without geometric superposition until they reach their final sizes with uniform size distribution under zero gravity and zero grain friction (Table 1—Formation method described in Bagi [4] and O'Sullivan [42]. Then interparticle friction and gravity are turned on. Finally, sediment compaction takes place as the vertical stress increases to 100 kPa under the zero-lateral strain boundary condition. In the free surface condition, the upper boundary is removed before dissolution starts. In some cases, we simulate granular interlocking due to grain angularity by hindering rotation on a preselected fraction of randomly distributed particles HR (Note: the validity of hindered rotation is explored in Mohamed and Gutierrez [38], and in Cha and Santamarina [9].

We simulate pressure solution through multiple particle size reduction steps, each followed by an equilibration stage. Each 2D-disk or 3D-sphere is shrunk by reducing its radius R proportionally to the total contact force ΣF_N acting on the particle. The relationship between dissolution rates (dR/dt) and contact forces (ΣF_N) is either linear $dR/dt = \alpha(\Sigma F_N)^1$ or quadratic $dR/dt = \alpha(\Sigma F_N)^2$. The quadratic model captures higher stress dependency. The size of all particles is updated in each i-th time step, $R_{i+1} = R_i - \alpha(\Sigma F_N)^\beta \cdot \Delta t$.

The proxy rate constant α is kept small and sufficient cycles—i.e., time-are allowed between size reductions to mimic natural dissolution without dynamic effects. In fact, the inertial number I, which describes the relative importance of inertia and confining stresses remains within the quasi-static criterion $I < 10^{-3}$ throughout the simulations [15, 37]. The ratio between the mean unbalanced force and the mean contact force remains smaller than 0.001 to ensure stable conditions. Multiple trials confirm that global and particle-scale simulation results are independent of α values when α is sufficiently small.

The proxy rate constant α and the exponent β are the same for all particles, and constant during dissolution. There is no reprecipitation and particles remain 2D-circular or 3D-spherical. The time step is set to $\Delta t = 0.6\sqrt{m/K}$ where *m* is the particle mass and *K* the particle stiffness; the time step changes as the grains mass *m* diminish during the simulations.

Table 1 Discrete element simulation environment—parametric study

	Properties	2D (disks)	3D (spheres)
Particle properties	Initial particle size (radius)	Uniform size distribution: $R_{min} = 0.4$ mm, $R_{max} = 0.6$ mm	Uniform size distribution: $R_{min} = 1$ mm, $R_{max} = 1.5$ mm
	Number of particles	10,567 disks	9167 spheres
	Density	2650 kg/m^3	2650 kg/m^3
	Inter-particle friction	0.5	0.5
	Hindered rotation HR	0% and 80%	0%
	Contact model	Linear contact model Normal stiffness $k_n = 10^8$ N/m Shear stiffness $k_s = 10^8$ N/m	Hertzian contact model Shear modulus $= 2.9 \times 10^9$ Pa Poisson's ratio = 0.3
Boundary conditions	Initial cell size	Height × Width: 10 cm × 10 cm	Height × Width × Length: 5 cm × 5 cm × 5 cm
	Vertical load	(1) 100 kPa (2) Self weight (open surface)	100 kPa
	Lateral boundaries	Zero strain	Zero strain
	Particle-to-wall friction	0	0
Dissolution rate versus contact force	Linear: $dR/dt = \alpha \cdot \Sigma F_N$ Quadratic: $dR/dt = \alpha \cdot (\Sigma F_N)^2$		

3 Results and analyses

The macro-scale evolution of the sediment and the history of particle scale information are recorded throughout the simulation. The simulations cease when internal processes or boundary measurements show steady changes, typically observed before a mass loss of ~ 20%.

3.1 Shear localization

Contact forces align preferentially in the vertical principal stress direction before dissolution, and there are evenly distributed force chains throughout. This situation changes during pressure solution: Fig. 1 shows contact force chains and strain fields after pressure solution (Note: strain fields are computed as the gradient of accumulated displacements from the beginning of dissolution). Shear bands spontaneously develop, for both linear and quadratic dissolution rates and in packings made of either free-rotating particles (HR = 0%) or interlocked particles (hindered rotation HR = 80%) (Fig. 1). Shear bands are 12–15 particles thick. Marked force chains form inside shear bands at a characteristic angle of ~ 50–60° with the shear band (case $dR/dt = \alpha \cdot F_N$ and HR = 0%). These strong force chains form and buckle as force-dependent dissolution progresses. Multiple weak, random slippages/localizations or dilations precede the emergence of the main shear bands (See the video—Supplementary Material). After the major localizations initiate, contact force chains in other parts homogenize more rapidly without experiencing temporal dilations. When

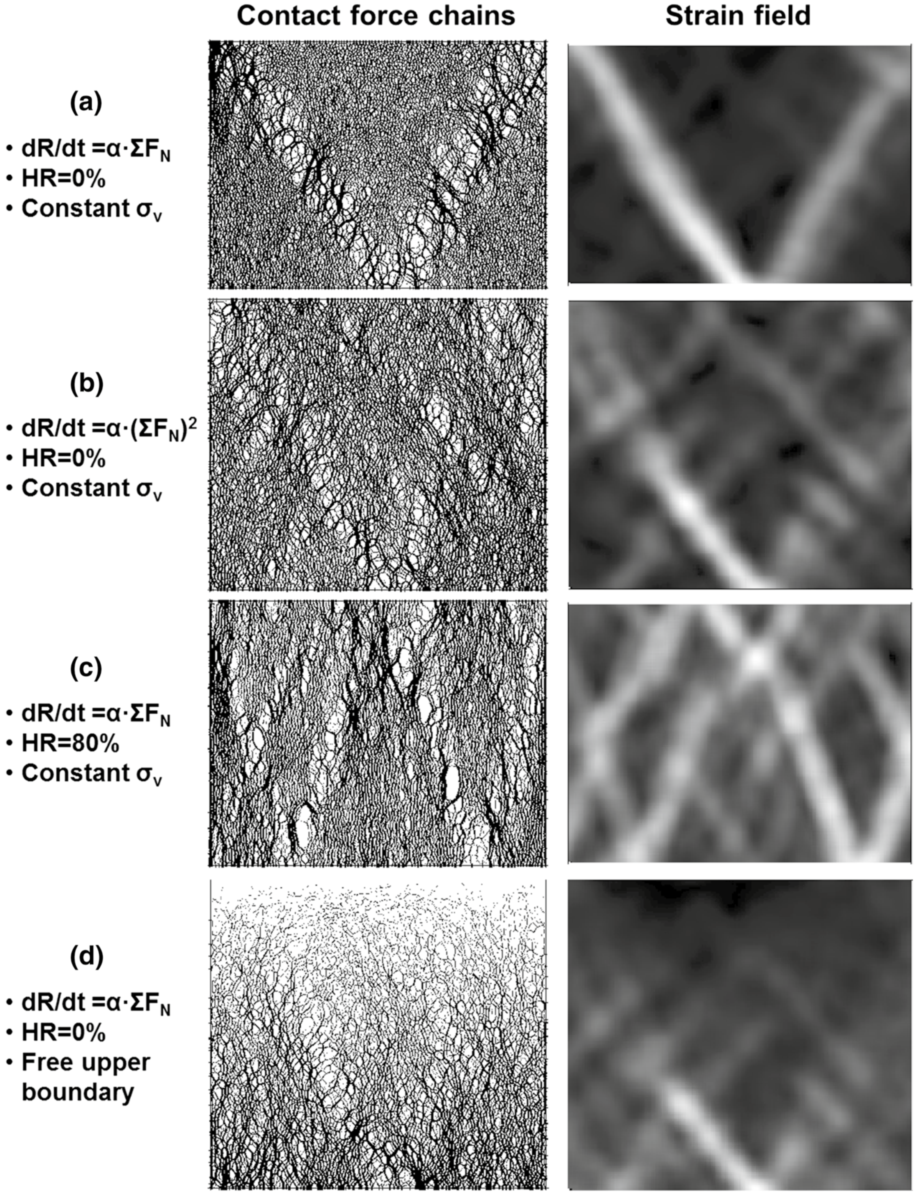

Fig. 1 Localized deformation: contact force chains and strain field. Data shown at the end of the simulation for different dissolution rates (β), degrees of interlocking HR and boundary conditions (Cases: 2D). Note: strain fields are based on displacements accumulated from the beginning of dissolution

there is a free upper boundary, shear localization is more pronounced at depth and diffuses towards the free surface because the dissolution process is contact-force dependent (Fig. 1d). For all cases, shear bands form in conjugate sets and tend to be symmetric. Shear bands form at steeper angles in packings with more interlocked particles, which agree with the higher global friction angle in granular materials with interlocking (Fig. 1c). The shear band angles approximately match $\beta = 45° + \phi/2$ for an internal friction angle of $\phi = 22°$ (for HR = 0%) and $\phi = 48°$ (for HR = 80%). Higher-stress dependency captured in the quadratic size-reduction relation leads to additional minor shear localizations (Fig. 1b) while keeping a similar shear-band angle ($45° + \phi/2$).

3.2 Vertical displacement: global contraction

The vertical displacement normalized by the initial specimen height is plotted versus the normalized mass loss $\Delta M/M_0$ defined as:

$$\frac{\Delta M}{M_0} = \frac{\sum R_{\mathrm{initial}}^2 - \sum R_{\mathrm{current}}^2}{\sum R_{\mathrm{initial}}^2} \quad \text{(for 2D disks)} \tag{1}$$

$$\frac{\Delta M}{M_0} = \frac{\sum R_{\mathrm{initial}}^3 - \sum R_{\mathrm{current}}^3}{\sum R_{\mathrm{initial}}^3} \quad \text{(for 3D spheres)} \tag{2}$$

Higher interlocking (HR = 80%) results in less vertical settlement, primarily due to the larger area occupied by shear bands, which have higher porosity (Fig. 2a). On the other hand, the size-reduction relationship has little effect on settlement. The normalized global vertical contraction increases almost linearly with the normalized mass loss in all cases (Fig. 2a), in agreement with relatively constant global porosities.

3.3 Porosity

The pre-dissolution global porosity (2D: n = 0.167, 3D: n = 0.399) decreases slightly during early stages of pressure solution as the granular packing evolves towards a more stable configuration (2D: n = 0.166, 3D: n = 0.398—both 2D and 3D cases correspond to linear dissolution rates and free rotation). Once the shear bands emerge, the local

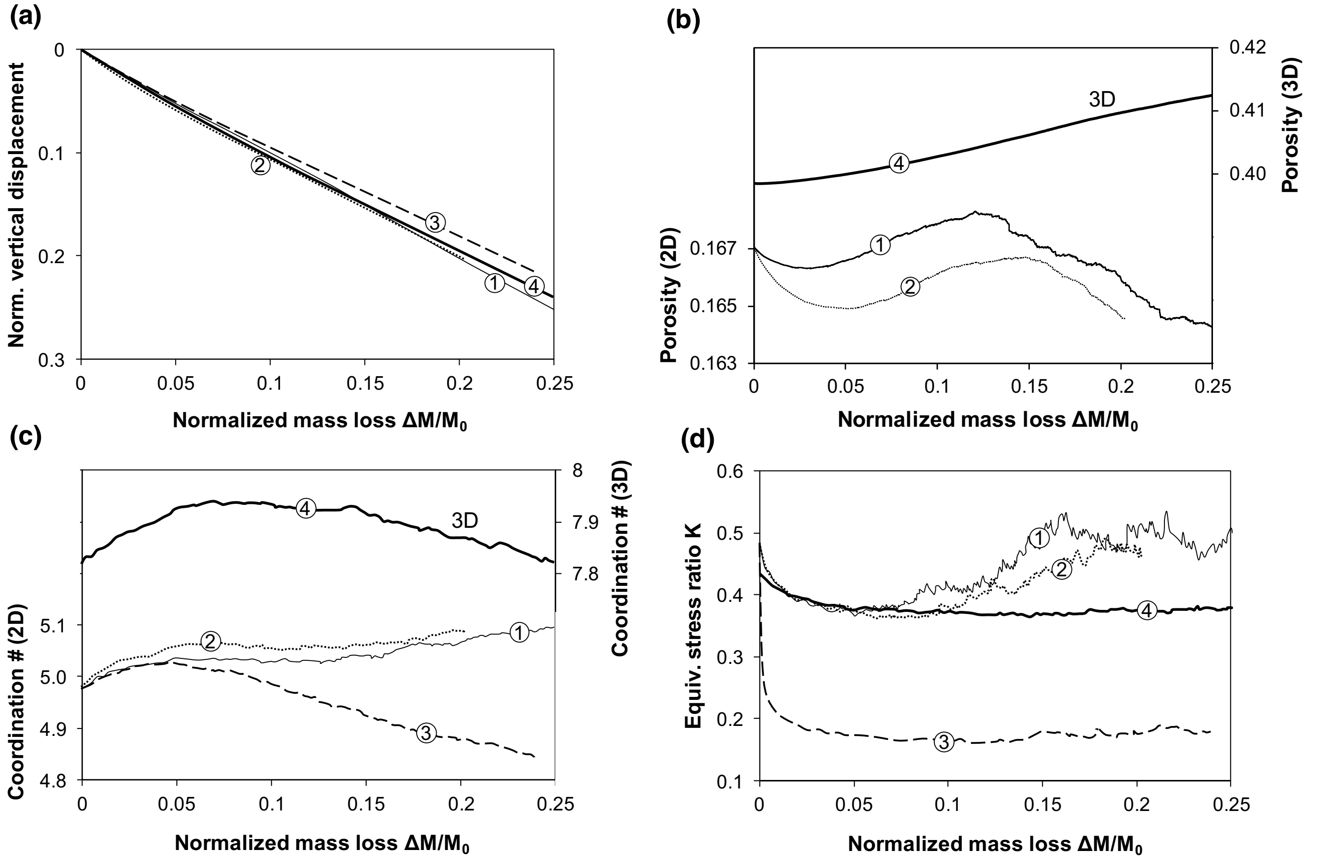

Fig. 2 Evolution of macroscale and grain-scale parameters during pressure-dependent dissolution. 2D and 3D cases. **a** Normalized vertical displacement, **b** global porosity, **c** global coordination number, **d** equivalent stress ratio K. Cases: ① $dR/dt = \alpha \cdot F_N$ and HR = 0% (2D) ② $dR/dt = \alpha \cdot F_N^2$ and HR = 0% (2D) ③ $dR/dt = \alpha \cdot F_N$ and HR = 80% (2D) ④ $dR/dt = \alpha \cdot F_N$ and HR = 0% (3D)

porosity increases in the shear band (2D: $n=0.191$ at $\Delta M/M_0=25\%$) while it decreases inside wedges (2D: $n=0.149$ at $\Delta M/M_0=25\%$ —Fig. 3). The combined effect for the whole 2D specimen is a small decrease in the global porosity ($n=0.164$ at $\Delta M/M_0=25\%$ —Fig. 2b). The global porosity increases monotonically in the 3D specimen ($n=0.413$ at $\Delta M/M_0=25\%$) because the relative volume occupied by shear localizations becomes larger than in the 2D case. The high porosity reductions, observed in nature are due to changes in particle shape as dissolved mineral species re-precipitate in the pore space. In addition, particle breakage does not occur in this simulation unlike in nature where particle breakage happens under shear, especially under high confining stress [18, 35].

3.4 Coordination number

The global coordination number slightly increases at the beginning of pressure solution as grain sizes adjust proportional to contact forces (Fig. 2c). Once shear bands form, the local coordination number decreases for particles in the shear band (see force chains in Fig. 1), while it increases in the wedges (Fig. 3). The global coordination number combines contacts within shear bands and wedges (Fig. 2c①, ②), and it decreases in sediments with high rotational frustration (see Fig. 2c③ for 2D with HR = 80% and Fig. 2c④ for the 3D specimen). Overall, the evolution in local and global coordination numbers parallels changes in porosity (Fig. 3). The global coordination numbers in Fig. 2c consider both virtual and real contacts, but the local coordination numbers in Fig. 3 consider real contacts only (Note: Virtual contacts correspond to interparticle separations less than 10^{-6} times the radius—the coordination number calculated using real contacts only may not satisfy the minimum coordination required for equilibrium).

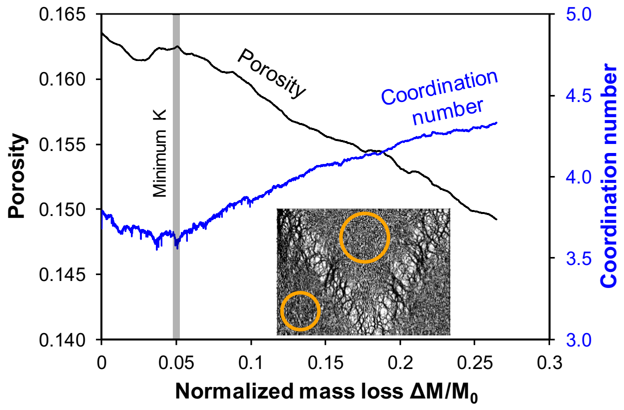

Fig. 3 Evolution of porosity and coordination number within wedges, away from shear bands (inside the orange measurement circles). Case: 2D, $dR/dt=\alpha\cdot F_N$ and HR = 0%

Before shear localization, the local coordination number oscillates (Fig. 3). The decrease of porosity and increase of coordination within the wedge is more evident after the shear localization (Fig. 3); this implies that the emergence of shear localization facilitates fabric homogenization in the wedges.

3.5 Equivalent global stress ratio K

The numerically computed equivalent stress ratio $K_0=\sigma_h/\sigma_v$ between vertical and horizontal stresses is $K_0=0.48$ before dissolution (Fig. 2d). The horizontal stress σ_h decreases during the early stages of pressure solution in all cases, typically for a mass loss $\Delta M/M_0<5\%$, and K_0 reaches a minimum value. Then, K_0 gradually recovers as dissolution proceeds. Previous studies report similar trends observed in homogeneous dissolution simulations and in experiments [9, 51]. As the minimum stress ratio is reached, there is marked force chain anisotropy and shear bands begin to develop. Granular interlocking allows higher force and fabric anisotropy and results in lower K values (Fig. 2d). Fluctuations in the equivalent global stress ratio K correspond to force chain formation and buckling.

3.6 Evolution of grain size distribution

Grain sizes satisfy a uniform distribution before pressure solution in all cases (Table 1). The size distribution shifts to smaller sizes and evolves towards a unimodal distribution during pressure solution (Fig. 4a). Changes in grain size couple with changes in contact forces (Fig. 4a, b). Furthermore, changes in particle relative sizes favor denser packing (Fig. 4b).

3.7 Interparticle forces

Pressure-dependent dissolution promotes contact force homogenization within wedges (Fig. 4b). The increase in coordination numbers and the homogenization of contact forces during pressure solution can be interpreted as “dissolving” springs in parallel: “force” dependent dissolution causes heavily loaded particles (or springs) to shorten and shed force to other particles that come into contact, i.e., the total number of springs in contact increases after pressure dissolution (Fig. 4b).

The polar plots of internal micromechanical parameters [46] show maximum fabric and contact force anisotropy when the stress ratio is minimum at the onset of localization (Fig. 5b). Pressure solution after shear localization leads to more isotropic global conditions within wedges.

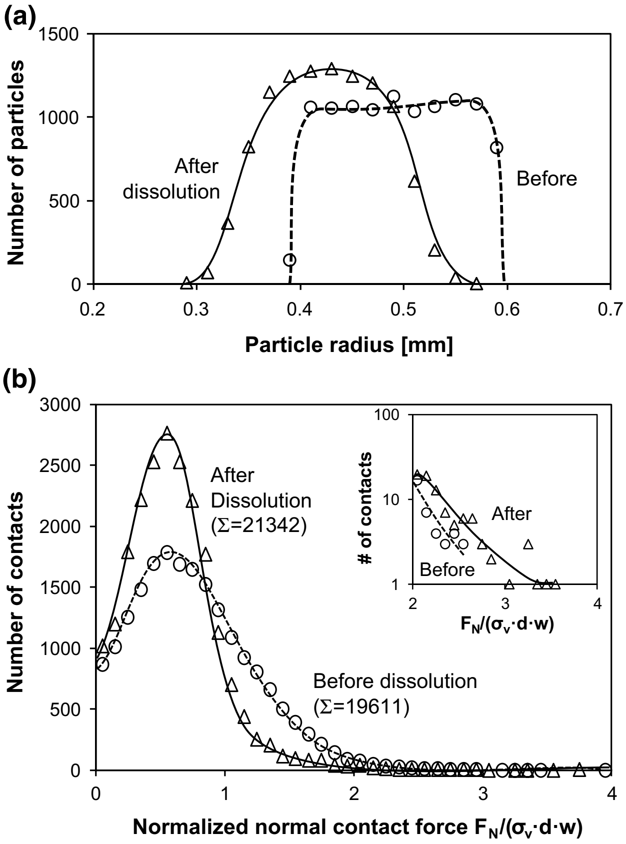

Fig. 4 Histograms of **a** particle size (Bin size = 0.02 mm) and **b** contact normal force before and after dissolution at $\Delta M/M_0 = 0.26$ (Bin size = 0.1). Case: 2D confined, $dR/dt = \alpha \cdot F_N$, and HR = 0%. The inset shows the tails of histograms for grains inside the shear band. Bin counts are connected to facilitate visualization

4 Discussion

Numerical simulations allow us to explore the macroscale implications of particle-level size reduction and to discern the sediment evolution during pressure solution.

4.1 Emergence of shear localization

During the early stage of pressure solution, the sediment evolves towards a dense granular structure that will tend to dilate upon shear because of its high coordination and low porosity; in the meantime, the horizontal stress decreases as seen in Fig. 2b–d. Eventually, the vertical-to-horizontal stress ratio σ_1/σ_3 reaches the Coulomb failure condition and the sediment experiences internal shear. The dilative and post peak strain softening behavior favors shear localization along shear bands [32, 47]. The local coordination number decreases and porosity increases inside the shear band, in a similar way to shear bands that form in biaxial or triaxial loading conditions [30, 43, 63].

There is no noticeable difference in particle size distribution within the shear band and in wedges outside the band. While high-contact force chains develop across the shear band, the highly loaded particles dissolve and readily transfer the load to neighboring particles that previously carried minimal loads.

There are no published reports of shear localization in one-dimensional loading under rigid lateral boundaries, including from tests specifically designed to explore pressure solution [19, 54, 61]. Lack of reporting may reflect the absence of shear bands when achieved strain levels are low (<5%) or that shear bands remained unnoticed as tests are conducted within rigid thick-wall cells. Certainly, shear localizations readily emerge in dilative soils under lateral relaxation as the stress ratio K drops to $K_{active} = (1 - \sin\phi)/(1 + \sin\phi)$. The reduction in stress ratio during dissolution under fixed lateral boundaries suggests the potential for dissolution-induced shear localization as observed in this study [9, 50].

4.2 A possible natural analogue: Polygonal faults

Seafloor sediments contain extensive polygonal fault systems [7]. Dissolution mechanisms have been suggested as a potential cause for the formation of these systems [51, 52]. Results presented in this study support this hypothesis and suggest that shear localization can emerge in normally consolidated sediments that experience pressure solution under zero-lateral strain boundary conditions. In agreement with the dissolution induced shear bands observed here, polygonal faults form at an angle $\beta \approx 45° + \phi/2$ from the horizontal. In addition, the general morphology of discontinuities in our simulation resembles the morphology of polygonal faults in the field [6, 33], such as the "ideal tier" V wedge (Fig. 1a) and the "complex tier" X wedge (Fig. 1c).

4.3 Differences in grain-scale dissolution

This study showed that pressure solution promotes early sediment densification even in the absence of reprecipitation. Away from shear bands, pressure-dependent dissolution decreases porosity, enhances particle coordination, and homogenizes contact forces; thus it is expected that the sediment becomes dilative and its strength increases. By contrast, previous studies have shown that the dissolution of randomly distributed soluble grains in a mixed-mineral packing causes an increase in porosity, the contact force fabric exhibits a honeycomb-like loose structure and the

Fig. 5 Polar plots of internal micromechanical parameters **a** before dissolution, **b** at minimum global stress ratio K, and **c** at the end of dissolution when $\Delta M/M_0 = 0.26$. Case: 2D confined, $dR/dt = \alpha \cdot F_N$ and HR = 0%. For comparison, see polar plots during deviatoric loading in Rothenburg and Bathurst [46]

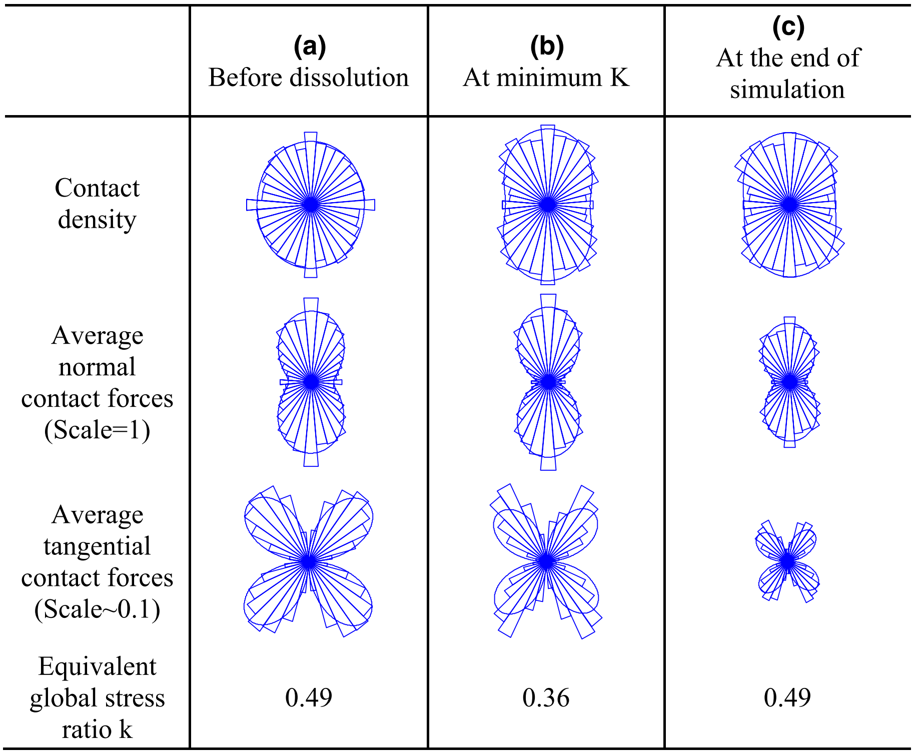

sediment becomes more compressible and weaker [8, 12, 50]; therefore, the sediment undergoes a marked decrease in shear stiffness [11, 24, 60] and loses mechanical strength [10, 59]. Therefore, the evolution of dissolution at the grain-scale can lead to pronounced differences in sediment responses at the macroscale.

4.4 Dissolution under isotropic-stress boundary

We also performed contact-force dependent dissolution under constant isotropic stress ($\sigma_o = 100$ kPa). In this case, the specimen contracts vertically and horizontally in equal amounts and the displacement vectors are concentric as the four boundaries close-in during dissolution; most importantly, results show no shear localization under these boundary conditions (Fig. 6). It follows that stress anisotropy may be a necessary condition for shear localization during pressure-dependent solution. Unlike the case of the zero-lateral strain boundaries under constant vertical loading, the porosity decreases and the coordination number increases monotonically (Fig. 7). Similarly to the cases ran with zero-lateral displacement boundaries,

Fig. 6 Pressure-dependent dissolution under isotropic stress boundary conditions. **a** Contact force chains and **b** displacement vectors at $\Delta M/M_0 = 0.18$

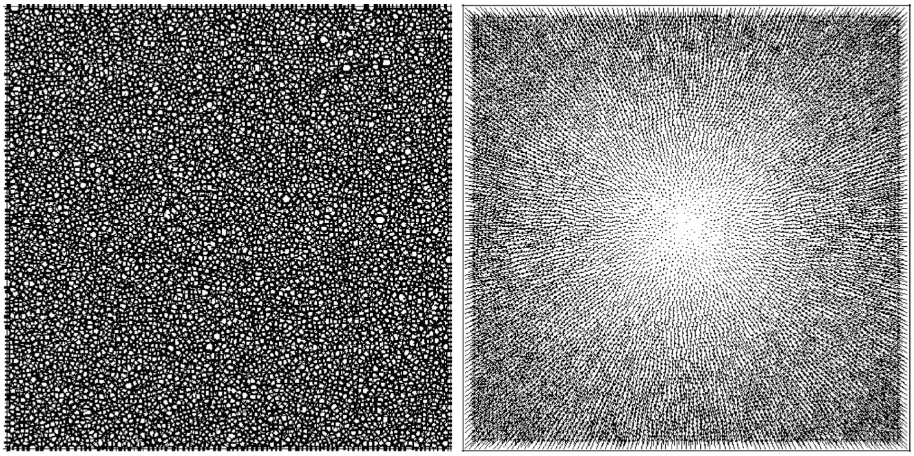

(a) Contact force chains. **(b)** Displacement vectors.

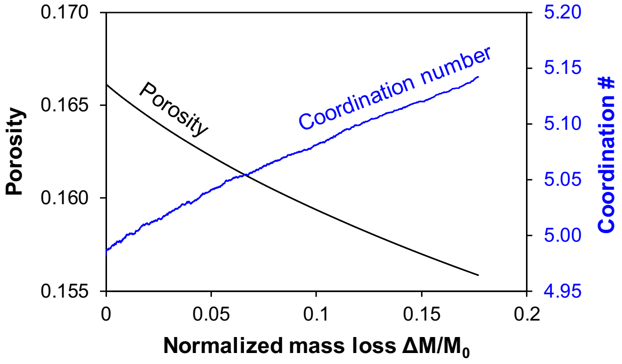

Fig. 7 Pressure-dependent dissolution under isotropic stress boundary conditions. The evolution of **a** global porosity and **b** coordination number versus mass loss. Case: 2D, Linear ($dR/dt = \alpha \cdot F_N$) and HR = 0%

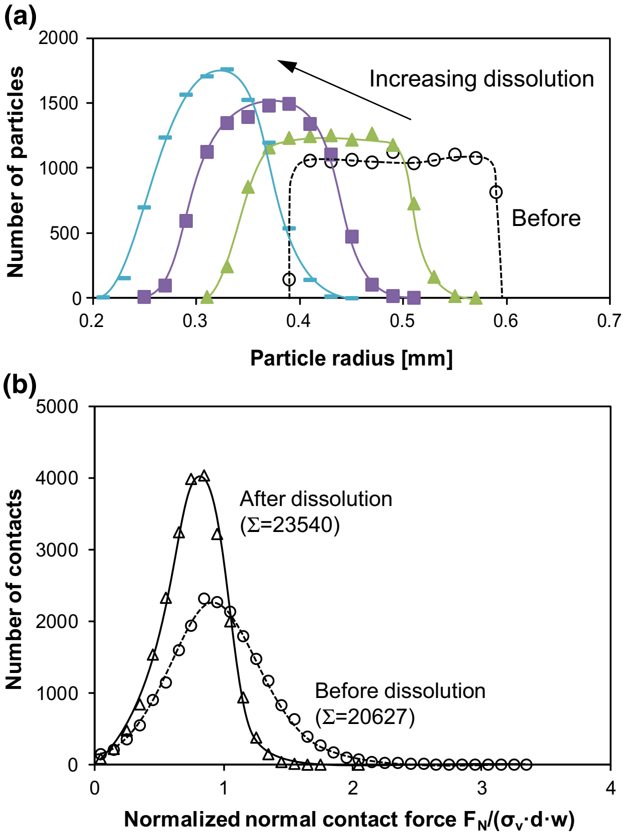

Fig. 8 Pressure-dependent dissolution under isotropic stress boundary conditions. Histograms of **a** particle size for various degrees of dissolution (Bin size = 0.02 mm) and **b** contact normal force before and after dissolution at $\Delta M/M_0 = 0.18$ (Bin size = 0.1). Case: 2D, Linear ($dR/dt = \alpha \cdot F_N$) and HR = 0%. Bin counts are connected to facilitate visualization

pressure-dependent dissolution promotes the unimodal distribution of particle sizes (Fig. 8a) and global contact force homogenization under isotropic stress conditions (Fig. 8b).

4.5 Limitations in particle- and pore-scale assumptions

These simulations emphasize the evolution of the granular skeleton rather than natural processes at the contact scale. In nature, the rate of dissolution is higher in the direction of the major principal stress hence particle shape changes with time; there is local reprecipitation and/or transport; the grain-to-grain contact area increases so the rate of pressure solution decreases in time; and small grains display faster pressure solution rates. In the simulations, particles remain 2D-circular or 3D-spherical; there is no precipitation but net mass loss; and there is no explicit size dependency. Therefore, the particle-level idealizations adopted in the numerical simulation deviate from the complex particle/pore scale processes in nature. Still, size reduction at the particle scale is the driver for changes in force equilibrium and internal kinetics that determine the effects observed above.

We also note that dissolution rates in the simulation are faster in smaller particles because the radius is reduced by the same amount for the same contact force as in larger particles. Furthermore, net mass loss may also take place in advective regimes where the pore fluid remains undersaturated in terms of dissolved species, such as near hill slopes, rivers, dams and embankments where the rate of transport exceeds the rate of reaction, i.e., low Damkohler number [1, 26].

5 Conclusions

We used the discrete element method to simulate the evolution of pressure-dependent mineral dissolution by gradual grain size reduction proportional to the total normal force carried by each grain.

All particles experience some size reduction. The initial uniform grain size distribution gradually becomes a unimodal distribution. While these simulations imply net mass loss, the porosity decreases in part due to the evolving grain size distribution but also due to the intimate packing that develops naturally from contact-force dependent dissolution.

Sediments experience an initial decrease in horizontal stress when pressure solution takes place under zero lateral strain boundary conditions. A shear band starts to emerge as the horizontal stress reaches the minimum value, and its inclination is a function of the angle of internal friction. Particles outside shear bands experience fabric and force homogenization, and densification, while particles within the shear band exhibit low coordination, pack at high porosity and develop marked contact-force chains.

Shear localization does not take place when pressure solution takes place under isotropic stress boundary conditions. Consequently, the stress anisotropy created by zero strain lateral boundaries provides a necessary condition for shear localization during pressure-dependent dissolution.

The development of shear localization during pressure solution may explain the presence of shear discontinuities and polygonal faults observed in level ground sediments in non-extensional and non-tectonic regions.

Acknowledgements Support for this research was provided by the Department of Energy Savannah River Operations Office, the Goizueta Foundation and the KAUST endowment. The authors are grateful to the anonymous reviewers for insightful comments. G. Abelskamp edited the manuscript.

Compliance with ethical standards

Conflict of interest The authors declare that they have no conflict of interest.

References

1. Alley, W.M., Healy, R.W., Labaugh, J.W., Reilly, T.E.: Flow and storage in groundwater systems. Science **296**, 1985–1990 (2002)
2. Angevine, C.L., Turcotte, D.L.: Porosity reduction by pressure solution—a theoretical-model for quartz arenites. Geol. Soc. Am. Bull. **94**, 1129–1134 (1983)
3. Angevine, C.L., Turcotte, D.L., Furnish, M.D.: Pressure solution lithification as a mechanism for the stick-slip behavior of faults. Tectonics **1**, 151–160 (1982)
4. Bagi, K.: An algorithm to generate random dense arrangements for discrete element simulations of granular assemblies. Granul. Matter **7**, 31–43 (2005)
5. Carrio-Schaffhauser, E., Raynaud, S., Latière, H.J., Mazerolle, F.: Propagation and localization of stylolites in limestones. Geol. Soc. Lond. Spec. Publ. **54**, 193–199 (1990)
6. Cartwright, J.: Diagenetically induced shear failure of fine-grained sediments and the development of polygonal fault systems. Mar. Pet. Geol. **28**, 1593–1610 (2011)
7. Cartwright, J., James, D., Bolton, A.: The genesis of polygonal fault systems; a review. Geol. Soc. Lond. Spec. Publ. **216**, 223–243 (2003)
8. Cha, M., Santamarina, J.C.: Predissolution and postdissolution penetration resistance. J. Geotech. Geoenviron. Eng. **139**, 2193–2200 (2013)
9. Cha, M., Santamarina, J.C.: Dissolution of randomly distributed soluble grains: post dissolution k_0-loading and shear. Géotechnique **64**, 828–836 (2014)
10. Cha, M., Santamarina, J.C.: Effect of dissolution on the load-settlement behavior of shallow foundations. Can. Geotech. J. **53**, 1353–1357 (2016)
11. Cha, M., Santamarina, J.C.: Hydro-chemo-mechanical coupling in sediments: localized mineral dissolution. Geomech. Energy Environ. **7**, 1–9 (2016)
12. Cha, M., Santamarina, J.C.: Localized dissolution in sediments under stress. Granul. Matter **21**, 79 (2019)
13. Croize, D., Bjorlykke, K., Jahren, J., Renard, F.: Experimental mechanical and chemical compaction of carbonate sand. J. Geophys. Res. Solid Earth **115**, B11204 (2010)
14. Cundall, P.A., Strack, O.D.L.: Discrete numerical-model for granular assemblies. Géotechnique **29**, 47–65 (1979)
15. da Cruz, F., Emam, S., Prochnow, M., Roux, J.-N., Chevoir, F.: Rheophysics of dense granular materials: discrete simulation of plane shear flows. Phys. Rev. E **72**, 021309 (2005)
16. de Boer, R.B.: On the thermodynamics of pressure solution—interaction between chemical and mechanical forces. Geochim. Cosmochim. Acta **41**, 249–256 (1977)
17. de Boer, R.B., Nagtegaal, P.J.C., Duyvis, E.M.: Pressure solution experiments on quartz sand. Geochim. Cosmochim. Acta **41**, 257–264 (1977)
18. de Bono, J.P., McDowell, G.R.: DEM of triaxial tests on crushable sand. Granul. Matter **16**, 551–562 (2014)
19. de Meer, S., Spiers, C., Peach, C.: Pressure solution creep in gypsum: evidence for precipitation reaction control. Phys. Chem. Earth **22**, 33–37 (1997)
20. Dewers, T., Hajash, A.: Rate laws for water-assisted compaction and stress-induced water–rock interaction in sandstones. J. Geophys. Res. Solid Earth **100**, 13093–13112 (1995)
21. Durney, D.W.: Solution-transfer, an important geological deformation mechanism. Nature **235**, 315–317 (1972)
22. Elliott, D.: Diffusion flow laws in metamorphic rocks. Geol. Soc. Am. Bull. **84**, 2645–2664 (1973)
23. Etheridge, M.A., Wall, V.J., Cox, S.F., Vernon, R.H.: High fluid pressures during regional metamorphism and deformation: implications for mass-transport and deformation mechanisms. J. Geophys. Res. **89**, 4344–4358 (1984)
24. Fam, M.A., Cascante, G., Dusseault, M.B.: Large and small strain properties of sands subjected to local void increase. J. Geotech. Geoenviron. Eng. **128**, 1018–1025 (2002)
25. Fowler, A.C., Yang, X.S.: Pressure solution and viscous compaction in sedimentary basins. J. Geophys. Res. Solid Earth **104**, 12989–12997 (1999)
26. Garven, G.: Continental-scale groundwater flow and geologic processes. Annu. Rev. Earth Planet. Sci. **23**, 89–117 (1995)
27. Gratier, J.P., Guiguet, R., Renard, F., Jenatton, L., Bernard, D.: A pressure solution creep law for quartz from indentation experiments. J. Geophys. Res. Solid Earth **114**, B03403 (2009)
28. Groshong, R.H.: Strain, fractures, and pressure solution in natural single-layer folds. Geol. Soc. Am. Bull. **86**, 1363–1376 (1975)
29. Hellmann, R., Gratier, J.P., Chen, T.: Mineral-water interactions and stress: pressure solution of halite aggregates. In: Arehart, G., Hulston, J. (eds.) Water–Rock Interaction, pp. 777–780. Balkema, Rotterdam (1998)
30. Iwashita, K., Oda, M.: Micro-deformation mechanism of shear banding process based on modified distinct element method. Powder Technol. **109**, 192–205 (2000)
31. Kuhn, M.R., Mitchell, J.K.: New perspectives on soil-creep. J. Geotech. Eng. ASCE **119**, 507–524 (1993)
32. Lade, P.V.: Instability, shear banding, and failure in granular materials. Int. J. Solids Struct. **39**, 3337–3357 (2002)
33. Lawrence, G.W.M., Cartwright, J.A.: The initiation of sliding on the mid Norway margin in the Møre Basin. Mar. Geol. **259**, 21–35 (2009)
34. Lehner, F.K.: A model for intergranular pressure solution in open systems. Tectonophysics **245**, 153–170 (1995)
35. Marone, C., Scholz, C.: Particle-size distribution and microstructures within simulated fault gouge. J. Struct. Geol. **11**, 799–814 (1989)
36. McDowell, G.R., Khan, J.J.: Creep of granular materials. Granul. Matter **5**, 115–120 (2003)
37. Midi, G.D.R.: On dense granular flows. Eur. Phys. J. E **14**, 341–365 (2004)
38. Mohamed, A., Gutierrez, M.: Comprehensive study of the effects of rolling resistance on the stress–strain and strain localization behavior of granular materials. Granul. Matter **12**, 527–541 (2010)

39. Niemeijer, A., Elsworth, D., Marone, C.: Significant effect of grain size distribution on compaction rates in granular aggregates. Earth Planet. Sci. Lett. **284**, 386–391 (2009)
40. Niemeijer, A., Marone, C., Elsworth, D.: Healing of simulated fault gouges aided by pressure solution: results from rock analogue experiments. J. Geophys. Res. Solid Earth **113**, B04204 (2008)
41. Niemeijer, A., Spiers, C.J., Bos, B.: Compaction creep of quartz sand at 400–600°C: experimental evidence for dissolution-controlled pressure solution. Earth Planet. Sci. Lett. **195**, 261–275 (2002)
42. O'Sullivan, C.: Particulate Discrete Element Modelling: A Geomechanics Perspective. Taylor & Francis, New York (2011)
43. Oda, M., Kazama, H.: Microstructure of shear bands and its relation to the mechanisms of dilatancy and failure of dense granular soils. Geotechnique **48**, 465–481 (1998)
44. Park, W.C., Schot, E.H.: Stylolites: their nature and origin. J. Sediment. Res. **38**, 175–191 (1968)
45. Raj, R.: Creep in polycrystalline aggregates by matter transport through a liquid-phase. J. Geophys. Res. **87**, 4731–4739 (1982)
46. Rothenburg, L., Bathurst, R.J.: Analytical study of induced anisotropy in idealized granular-materials. Geotechnique **39**, 601–614 (1989)
47. Rudnicki, J.W., Rice, J.R.: Conditions for localization of deformation in pressure-sensitive dilatant materials. J. Mech. Phys. Solids **23**, 371–394 (1975)
48. Rutter, E.H.: Pressure solution in nature, theory and experiment. J. Geol. Soc. **140**, 725–740 (1983)
49. Shimizu, I.: Kinetics of pressure solution creep in quartz—theoretical considerations. Tectonophysics **245**, 121–134 (1995)
50. Shin, H., Santamarina, J.C.: Mineral dissolution and the evolution of k_0. J. Geotech. Geoenviron. Eng. **135**, 1141–1147 (2009)
51. Shin, H., Santamarina, J.C., Cartwright, J.A.: Contraction-driven shear failure in compacting uncemented sediments. Geology **36**, 931–934 (2008)
52. Shin, H., Santamarina, J.C., Cartwright, J.A.: Displacement field in contraction-driven faults. J. Geophys. Res. Solid Earth **115**, B07408 (2010)
53. Sibson, R.H.: Earthquakes and rock deformation in crustal fault zones. Annu. Rev. Earth Planet. Sci. **14**, 149–175 (1986)
54. Spiers, C., Schutjens, P., Brzesowsky, R., Peach, C., Liezenberg, J., Zwart, H.: Experimental determination of constitutive parameters governing creep of rocksalt by pressure solution. Geol. Soc. Lond. Spec. Publ. **54**, 215–227 (1990)
55. Sprunt, E.S., Nur, A.: Destruction of porosity through pressure solution. Geophysics **42**, 726–741 (1977)
56. Tada, R., Siever, R.: Pressure solution during diagenesis. Annu. Rev. Earth Planet. Sci. **17**, 89–118 (1989)
57. Terzaghi, K., Peck, R.B., Mesri, G.: Soil Mechanics in Engineering Practice, 3rd edn. Wiley-Interscience, Hoboken (1996)
58. Toussaint, R., Aharonov, E., Koehn, D., Gratier, J.P., Ebner, M., Baud, P., Rolland, A., Renard, F.: Stylolites: a review. J. Struct. Geol. **114**, 163–195 (2018)
59. Tran, M.K., Shin, H., Byun, Y.-H., Lee, J.-S.: Mineral dissolution effects on mechanical strength. Eng. Geol. **125**, 26–34 (2012)
60. Truong, Q.H., Eom, Y.H., Lee, J.S.: Stiffness characteristics of soluble mixtures. Géotechnique **60**, 293–297 (2010)
61. Visser, H., Spiers, C., Hangx, S.: Effects of interfacial energy on compaction creep by intergranular pressure solution: theory versus experiments on a rock analog (NaNO3). J. Geophys. Res. Solid Earth **117**, B11211 (2012)
62. Yasuhara, H., Marone, C., Elsworth, D.: Fault zone restrengthening and frictional healing: the role of pressure solution. J. Geophys. Res. Solid Earth **110**, B06310 (2005)
63. Zhou, W., Yang, L., Ma, G., Xu, K., Lai, Z., Chang, X.: DEM modeling of shear bands in crushable and irregularly shaped granular materials. Granul. Matter **19**, 25 (2017)